Plasmon-Enhanced Optical Trapping of Gold Nanoaggregates with Selected Optical Properties

Elena Messina,[†] Emanuele Cavallaro,[‡,§] Adriano Cacciola,[‡,⊥] Maria Antonia Iatì,[‡] Pietro G. Gucciardi,[‡] Ferdinando Borghese,[§] Paolo Denti,[§] Rosalba Saija,[§] Giuseppe Compagnini,[†] Moreno Meneghetti,[¶] Vincenzo Amendola,[¶] and Onofrio M. Maragò[‡,*]

[†]Dipartimento di Scienze Chimiche, Università di Catania, I-95125 Catania, Italy, [‡]CNR-Istituto per i Processi Chimico-Fisici, I-98158 Messina, Italy, [§]Dipartimento di Fisica della Materia e Ingegneria Elettronica, Università di Messina, I-98166 Messina, Italy, [⊥]Dipartimento di Fisica, Università di Messina, I-98166 Messina, Italy, and [¶]Dipartimento di Scienze Chimiche, Università di Padova, I-35131 Padova, Italy

ABSTRACT We show how light forces can be used to trap gold nanoaggregates of selected structure and optical properties obtained by laser ablation in liquid. We measure the optical trapping forces on nanoaggregates with an average size range 20−750 nm, revealing how the plasmon-enhanced fields play a crucial role in the trapping of metal clusters featuring different extinction properties. Force constants of the order of 10 pN/nmW are detected, the highest measured on a metal nanostructure. Finally, by extending the transition matrix formalism of light scattering theory to the optical trapping of metal nanoaggregates, we show how the plasmon resonances and the fractal structure arising from aggregation are responsible for the increased forces and wider trapping size range with respect to individual metal nanoparticles.

Understanding the properties and extending the handling strategies for plasmonic structures of different size and shape is nowadays of primary importance for basic and applied research as well as for modern technology.[1] Electronics, photonics, catalysis, and biomedicine are among the most relevant research fields in which metal colloids as well as ordered nanoparticle arrays are employed either macroscopically or at the nanometer scale.[2] Because of such an increasing request, researchers are continuously stimulated to find new solutions and develop original strategies for the production, isolation, and control of such intriguing nano-objects.[3−8] Moreover aggregation among metal particles in colloidal systems offers the opportunity to study fundamental aspects in surface-enhanced Raman spectroscopy (SERS)[9,10] and in plasmonics[2] since rough or fractal surfaces give a strong coupling of the single particle induced electric field, generating the so-called "hot spots".[9−11] The possibility to isolate individual aggregates gives the opportunity to perform the analysis or the amplification on clusters of specific selected optical and electric properties.

Optical tweezers[12] (OT), tools for the trapping and manipulation of micro-[13,14] and nanoparticles,[15−20] have led to a real optical revolution[14] in physics, chemistry, material sciences, and biology. When used as a force transducer, OT can measure forces at the femtonewton;[15,17] their recent integration with Raman spectroscopy (Raman tweezers) allowed for ultrasensitive chemical−physical analysis of trapped particles.[21,22] OT have been used to hold and manipulate individual metal nanoparticles since the pioneering work of Svoboda and Block.[23] Light forces scale with particle volume,[15,23]

hence manipulating nanoparticles with optical tweezers is generally difficult, because Brownian motion can easily overwhelm the trapping forces. On the other hand the occurrence of plasmon resonances in metal nanoparticles is the key for enhancing light forces that can stably hold particles as small as 10−20 nm in size.[24−36] Indeed plasmon-enhanced forces and torques have been used to trap and align nanorods[19,26,28] and bipyramids[32] for all-optical patterning of surfaces.[33] Moreover, both trapping and repulsive optical forces have been shown to operate on metal nanoparticles depending on size[34] and detuning,[35] demonstrating the crucial role played by the plasmon resonance in these systems. However only a specific size range has been shown to be trappable in optical tweezers because spherical particles with a size larger than 250 nm have increased absorption that pushes them out of the confining light field.[24,29,30] Metal

©2011 American Chemical Society
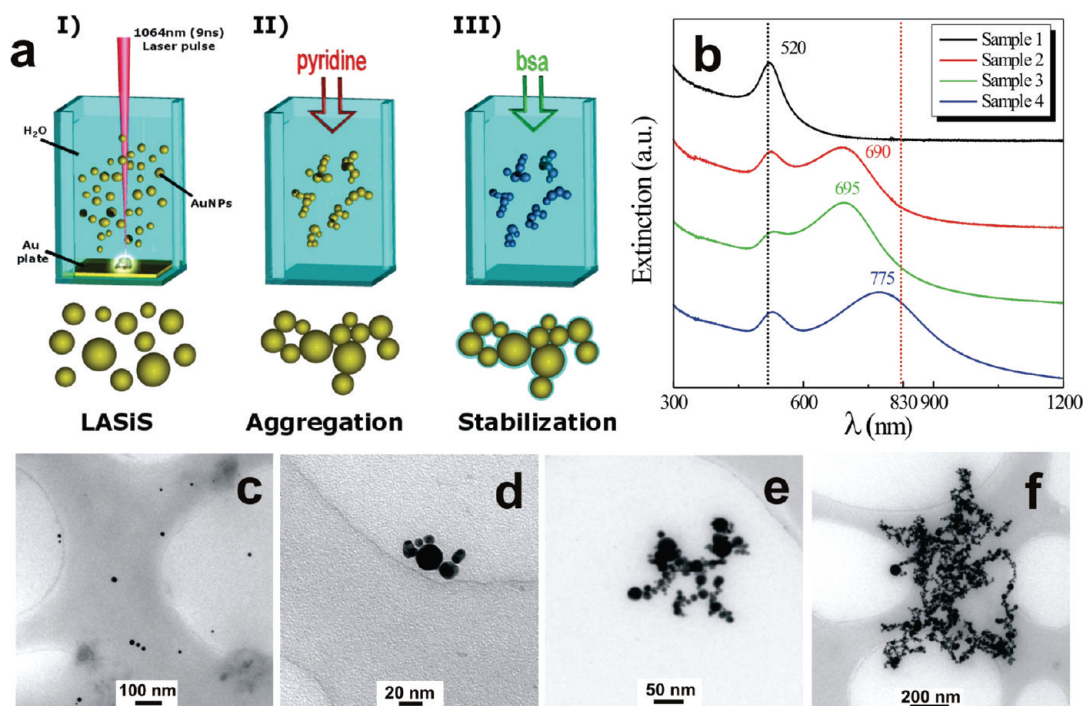
Figure 1. (a) Sketch of the three step procedure for the preparation of AuNPAs: (I) LASiS; (II) aggregation with pyridine; (III) stabilization with BSA. (b) Extinction spectra for the different samples of gold nanoaggregates obtained by laser ablation in water and after the three-step procedure described in panel a. Sample 1 (black line) is composed of individual nanoparticles with no aggregation. Sample 2 (red line), sample 3 (green line), and sample 4 (blue line) are obtained by adding increasing amounts of pyridine to AuNPs solutions. Note that each spectrum in the graph has been offset from the origin of the y-axis to make the plots more visible. (c—f) TEM images taken for nonaggregated AuNPs (c, sample 1) and for AuNPAs with different aggregation levels (d, sample 2; e, sample 3; f, sample 4), corresponding to different average sizes of aggregates.

aggregates have been qualitatively shown to be influenced by optical forces,[19,37,38] but this has been demonstrated close to a surface where radiation pressure is neglected and in extreme experimental conditions in the presence of laser-induced heating.[37,38]

Here we measure optical forces on functionalized gold nanoaggregates with controlled extinction properties and different average radii in the 20—750 nm range, obtained by laser ablation in liquid, showing how optical trapping efficiencies are enhanced 50 times with respect to forces measured on individual gold spherical particles. We also develop a full electromagnetic theory of optical trapping of metal nanoaggregates, showing how aggregation yields increased forces and wider trapping size range with respect to individual metal nanoparticles.

RESULTS AND DISCUSSION

Gold Nanoaggregates with Controlled Extinction. Plasmonic nanostructures with controlled extinction properties have been obtained *via* a three step procedure (see Methods). In the first step, gold nanoparticles (AuNPs) with an average diameter of 35 nm were produced in water by laser ablation synthesis in solution (LASiS), according to the protocol[39,40] sketched in Figure 1a, consisting in the laser ablation (1064 nm, 9 ns, 10 Hz laser pulses) of a pure gold target (99.99%) dipped in a solution of bidistilled water.[39] LASiS is a "green" method that does not require any chemicals or other stabilizing

agents because so obtained AuNPs have a negative surface charge due to partial surface oxidation (about 5% of surface atoms) and form a colloidal system indefinitely stable in time.[41] In the second step, we added variable amounts of pyridine to three different AuNPs solutions to promote particles aggregation (Figure 1a). Pyridine is known to bind gold surface through the nitrogen lone-pair electrons, promoting particles aggregation.[42,43] The stability of the colloidal system is dependent on the pyridine concentration, with larger amounts of pyridine corresponding to larger particle aggregation.[42,43] In the third step, the aggregation process was frozen by adding bovine serum albumin (BSA) to the AuNPs aggregates (AuNPAs in the following) 30 min after pyridine addition, exploiting the high conjugation ability of BSA for AuNPs obtained by LASiS.[39] UV—visible spectra (Figure 1b) of the four AuNP solutions show that a sharp absorption band at 525 nm is observed for nonaggregated spherical AuNPs (sample 1) and that a second red-shifted band appears in samples 2, 3 and 4, that is a clear indication that particles aggregation took place.[9] UV—vis spectra show that aggregation was larger for larger amounts of pyridine added to AuNPs, since a larger red shift and a larger optical density of the second plasmon resonance band are observed going from sample 2 to sample 4. Therefore, controlling particles aggregation is a simple way to control the plasmonic properties of such gold nanostructures. We have
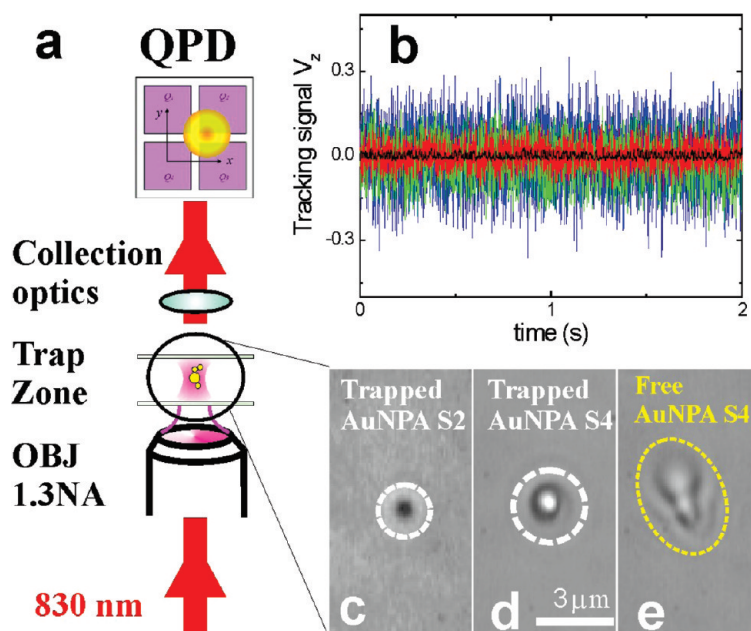
Figure 2. (a) Sketch of the optical trapping setup. A NIR laser beam is focused by a 1.3 NA oil immersion microscope objective. Particles trapped in a water dispersion were AuNPAs produced by LASiS. The scattered light from the trapped particle is detected by a QPD through a collection optics yielding electrical signals proportional to the particle displacements. (b) Tracking signals as acquired from the QPD for a trapped AuNP from sample 1 (black trace), a trapped AuNPA from sample 2 (red trace), sample 3 (green trace), and sample 4 (blue trace). (c–e) CCD images of optically trapped AuNPAs from sample 2 (c) and sample 4 (d). In panel c the size of the nanoaggregate is smaller than the diffraction limit of the imaging system. In panel d the nanoaggregate is aligned with the propagation axis having an extent of about 2 μm. This is revealed when the laser is switched off (e) and the same aggregate is untrapped and free floating away from the trap.

used transmission electron microscopy (TEM) for investigating the structure of the AuNPAs in samples 1–4. The analysis of more than 60 TEM images shows spherical nanoparticles with average size of about 35 ± 10 nm before aggregation (sample 1), and fractal structures with average size of 90 ± 30, 250 ± 50, and 750 ± 250 nm for the aggregated samples 2, 3, and 4, respectively. The uncertainty on these values represents the standard deviation from the measured average size. Representative TEM images of the four samples are reported in Figure 1c–f. The fractal structure of the clusters is typical of diffusion limited aggregation (DLA) processes.[44]

Optical Trapping. Optical trapping is obtained in an experimental setup with an inverted configuration,[17,19] that is, the trapping laser propagates upward (Figure 2a and Methods). The light from a near-infrared laser diode (830 nm) is focused by an oil immersion microscope objective with a high numerical aperture (NA = 1.3) in a sample chamber. The available maximum power at the sample is about 32 mW, but during force measurements of optically trapped AuNPAs it was limited to 15 mW. In fact, when using maximum power we observed strong heating[36] and bubbling[37] while trapping large (micro) aggregates from samples 3 and 4 (see video in Supporting Information). In Figure 3a–d we show an image sequence of a bubble growth soon after a microaggregate from sample 3 is drawn into the trap; the bubble growth lasts a few seconds, until the bubble reaches a size of about 5–6 μm and the growth stops. In sample 4 we observed growth of larger

bubbles (20–30 μm) indicating a larger heating of the water surrounding the aggregates (Figure.3e,f).

In our optical setup the same objective allows the imaging of the trapped nano- and microparticles onto a CCD camera. Figure 2 panels c and d show images of AuNPAs from sample 2 and sample 4, respectively, optically trapped at low power. In Figure 2c the size of the nanoaggregate is smaller than the diffraction limit of the imaging system. In Figure 2d the aggregate is aligned with the propagation axis[18,45] having a longitudinal extent at the micrometer scale (about 2 μm). This is revealed when the laser is switched off (Figure 2e) and the same aggregate is untrapped and free floating away from the trap. Moreover continuous rotation in the optical trap is observed for AuNPAs with a strong asymmetric morphology[19] (see video in Supporting Information). The rotation is a consequence of the particle shape; that is, anisotropic scattering causes rotation about the laser propagation direction[46] (the so-called "windmill effect").

We perform radiation force measurements always with no rotation driven on the trapped particle. The distance from the coverslip is kept much larger than the particle average size, in the range 4–14 μm, where stable trapping is always ensured and the hydrodynamic perturbation of the bottom surface is negligible. Forces on trapped AuNPAs are measured through particle tracking (see Methods) and Brownian motion analysis[15,47] of the signals S_x, S_y, S_z from a quadrant photodiode (QPD) proportional to the trapped particle's displacements in the three spatial directions (x, y, z)
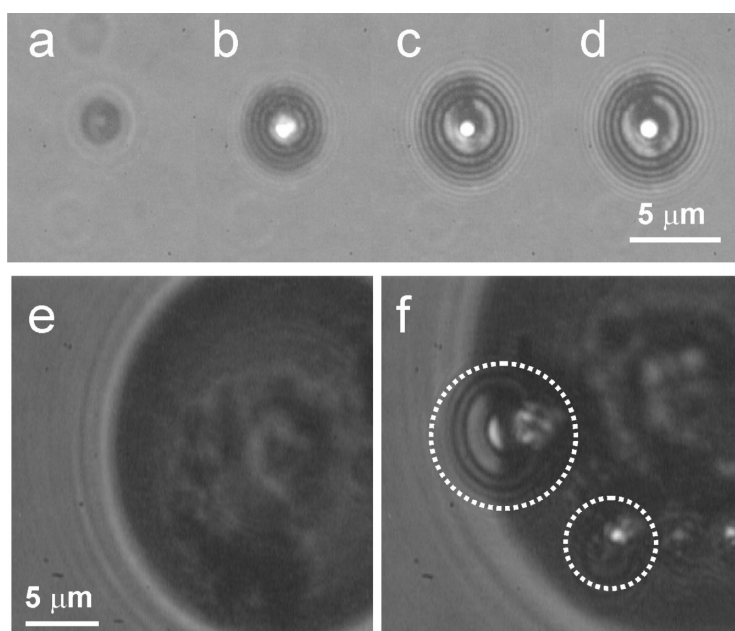
Figure 3. Heating of trapped large AuNPAs from samples 3 and 4 at high laser power (32 mW at the sample) and consequent bubbling. We trap few micrometers away from the coverslip surface and as soon as the bubble is formed the suspension collapses and the bubble grows on the surface. The heating around the aggregate increases further because of the change of the surrounding fluid and makes the bubble to grow even further up to a scale of tens of micrometers. (a–d) Image sequence of bubble formation and growth around a trapped aggregate from sample 3. (e) A bubble formed around a large AuNPA in sample 4 draws other AuNPs in the region on the water–vapor interface. (f) Optical trapping of these particles at the interface yields laser heating that generates secondary bubbles (dashed circles).

defined by the trapping potential. Figure 2b shows some representative particle tracking signals for trapped AuN-PAs in the different samples. An increase in the dimension of the trapped AuNPAs results in a larger amplitude of the recorded fluctuating signals. Moreover we ensure that only one particle is trapped during each measurement by looking simultaneously at the CCD camera images and at the tracking signals. If an additional particle would fall in the trap during an experiment this would be clearly visible on both the CCD camera and on the interferometric pattern of the tracking signals shown in Figure 2b.

The starting point of force sensing with optical tweezers is the Langevin equation in the confining harmonic potential[15,17] $V(x) = \sum {}^1/_2 k_i x_i^2$, with k_i being the spring constants. For a trapped particle with an hydrodynamic radius r this can be written as

$$\partial_t x_i(t) = -\omega_i x_i(t) + \xi_i(t), \quad i = x, y, z \quad (1)$$

Where the relaxation frequency $\omega_i = k_i/\gamma$ is related to the force constants and hydrodynamic (viscous) damping $\gamma = 6\pi\eta r$ (Stokes' law), η being the dynamic viscosity of water. The terms $\xi_i(t)$ describe random uncorrelated fluctuations with zero mean $\langle\xi_i(t)\rangle = 0$ and $\langle\xi_i(t)\,\xi_j(t + \tau)\rangle = 2D\cdot\delta(\tau)\delta_{ij}$, where the angled brackets indicate a time-averaged quantity and $D = k_BT/\gamma$ is the diffusion constant (Einstein's relation) dependent on temperature T and damping.[15] To get the spring constants from experimental particle tracking signals, we use a time domain analysis[17,19] of the thermal fluctuations in the trap by looking at their autocorrelation

functions[15] $C_{ii}(\tau) = \langle x_i(t)\, x_i(t + \tau)\rangle$. This method has been shown to be very successful for accurate measurements of optical forces[48] and torques,[17,49] hydrodynamic interactions,[50] and optically induced rotations.[19] From eq 1 autocorrelations obey first order uncoupled differential equations with the lag time τ, that can be easily integrated giving exponential decays with relaxation frequencies ω_i and zero point value $C_{ii}(0) = k_BT/\gamma\omega_i$. Typical autocorrelation analysis of the tracking signals for a trapped AuNPA from sample 2 is shown in Figure 4. By fitting these data with an exponential decay we get the relaxation rates $\omega_x = (5010 \pm 70)$ s^{-1}, $\omega_y = (6500 \pm 100)$ s^{-1}, $\omega_z = (620 \pm 5)$ s^{-1}. We now calculate the hydrodynamic damping coefficient from the Stokes' law by approximating the nanoaggregate hydrodynamic radius to the average radius $r = 45 \pm 15$ nm obtained from several TEM images of AuNPAs in sample 2. Thus $\gamma = (0.77 \pm 0.25)$ fN·s/μm and the corresponding spring constants for this specific data are $k_x = (3.9 \pm 1.3)$ pN/μm, $k_y = (5.0 \pm 1.7)$ pN/μm, $k_z = (0.48 \pm 0.15)$ pN/μm. The error on these values takes into account the approximation and deviation on the size of the aggregate coming from TEM analysis that propagates through the damping coefficient. Despite that the spherical approximation might seem too extreme for the larger and more asymmetric aggregates, we note that even a factor of 5 in the asymmetry (estimated as the ratio of longer to shorter axis of the aggregate) only changes the hydrodynamic damping by only 10%.[17,51] Thus we followed the same procedure
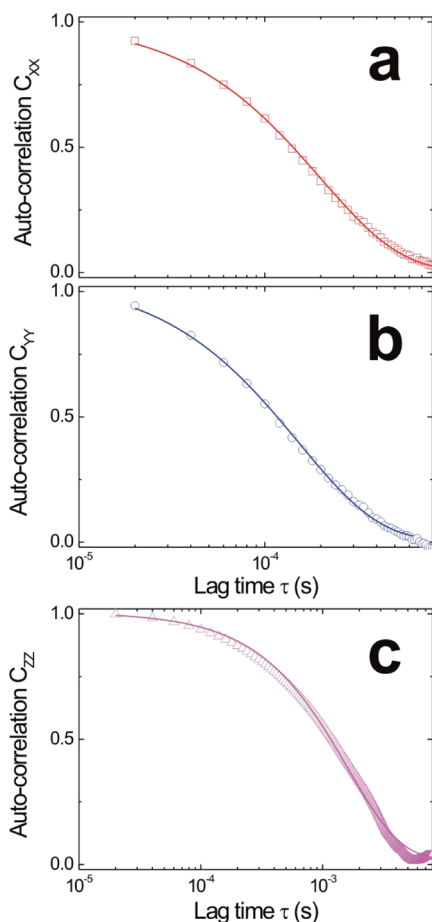
Figure 4. Normalized autocorrelation functions of the tracking signals along the polarization x-axis (a), y-axis (b), and propagation z-axis (c) for a gold nanoaggregate from sample 2. The data are well fitted with an exponential function with deacay rates $\omega_x = (5010 \pm 70)$ s^{-1}, $\omega_y = (6500 \pm 100)$ s^{-1}, $\omega_z = (620 \pm 5)$ s^{-1}. **These values yield the force constants of** $k_x = (3.9 \pm 1.3)$, $k_y = (5.0 \pm 1.7)$, $k_z = (0.48 \pm 0.15)$ **pN/μm as explained in the text.**

for all our samples and studied the general behavior of the radiation force with the increase of aggregation. We trapped and analyzed 10 different aggregates for each sample and averaged the resulting relaxation frequencies and spring constants. The trapped aggregates where selected randomly to measure the average optical force on each sample and to ensure that no bias would affect our measurements. The results are shown in Figure 5. In Figure 5a we plot the autocorrelation decay rates as a function of the lower energy plasmon resonance wavelength measured from extinction (Figure 1b). The uncertainty on the relaxation rates represents the standard deviation on the measurements for each sample. We then show in Figure 5 panels b, c, and d the force constants normalized to power k_i/P, that is, a measure of the optical trapping efficiency, as a function of the average radius of the AuNPAs for each sample. Both decay rates and spring constants along the optical (z-)axis are lower than the ones in the transverse plane and the spring constants

along the polarization (x-)axis are lower than the ones along the y-direction, as we expect because of the focusing properties of a linearly polarized laser beam at the diffraction limit.[18,30] The measured force constants for the aggregates (red, green, blue data) are between 50 and 1000 times larger than the values measured for their constituents spherical AuNPs in sample 1 (black data). Moreover for AuNPAs in sample 4 with an average size of about 750 nm we measured force constants as high as 10 pN/nmW, a value 50 times larger than the maximum value reported in experiments with the largest ($r = 127$ nm) gold spherical particles[24,29,30] (yellow region in Figure 5b–d).

Theory. Light forces are generated by the scattering of electromagnetic fields incident on a particle. For a quantitative understanding of optical trapping we rely upon the scattering theory of electromagnetic radiation.[52] The models traditionally used for calculating optical forces are based on approximations which often limit the discussion only to spherical particles. Instead, to have some more indications on the role of aggregation in plasmon-enhanced optical trapping, we calculate the radiation force on gold nanoaggregates by extending the full scattering theory in the framework of the transition matrix (T-matrix) approach[18,53] (see Methods), recently successfully used for accurate comparison with experiments on spherical metal nanoparticles.[30] The T-matrix formalism is quite general, it applies to particles of any shape and refractive index, and for any choice of incident wavelength relative to particle size.[52]

In Figure 5 panels b–d we first compare the measured force constants with the theoretical values predicted for spherical AuNP at our trapping wavelength (purple solid line), finding a very good agreement between theory and experiments for data of sample 1. Thus we modeled AuNPAs as clusters of spherical subunits. The dimensions of each subunit are chosen in the range measured from TEM images and so that the wavelength of the lower energy plasmon resonance of the whole cluster is close to the measured value (see Figure 6). The experimental aggregation process is obtained through a coating with pyridines molecules, for this reason in our models the single spheres are not in mutual contact, but separated by a very small distance of about 0.5 nm. Moreover we used the optical constants for gold measured by Johnson & Christy.[54] The use of such constants in the modeling of aggregates poses several critical issues due to the lack of convergence in the multipole expansion.[52] For this reason, we introduced the longitudinal dielectric function, described by Lindhard,[55] as reported and simplified by Pack.[56] We investigated the optical properties of several gold aggregates, built so to satisfy the requirements described above. As an example, we show in Figure 6a three different models of clusters inspired to the TEM images of sample 2 AuNPAs. In Figure 6b are reported the corresponding extinction
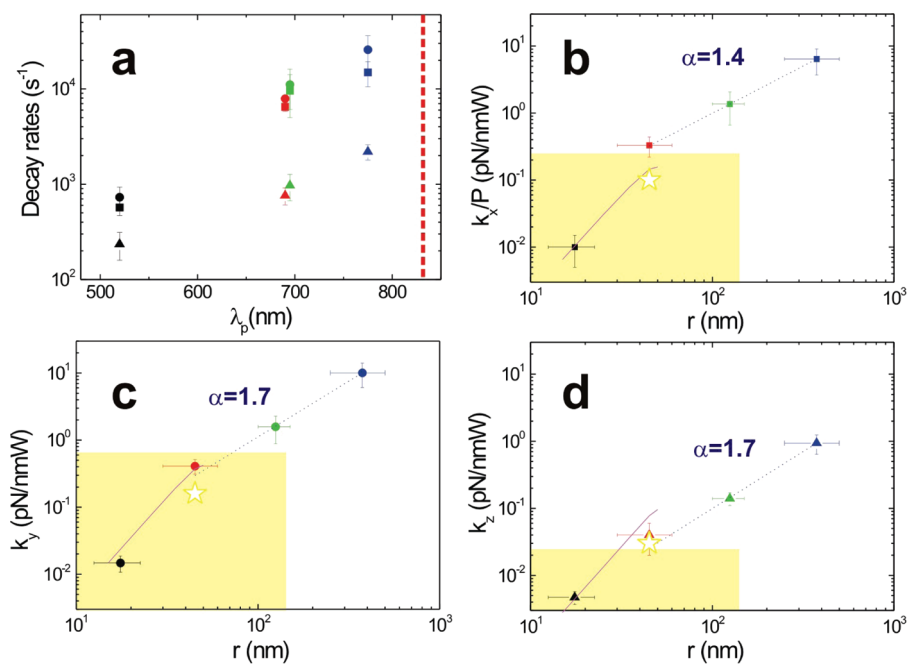
Figure 5. (a) Autocorrelation decay rates ω_x (squares), ω_y (circles), and ω_z (triangles) as a function of the plasmon resonance peak wavelength λ_p. Black symbols are related to the nonaggregated sample 1 with resonance at 520 nm, while red, green, and blue are related to samples 2, 3, and 4, respectively, with higher aggregation and a longer wavelength plasmon peak. The vertical red line identifies the trapping wavelength at 830 nm always red-shifted from resonance. The plotted values are averaged over measurements on 10 different gold nanostructures in each sample. Error bars are the standard deviation over these measurements. In panels b, c, and d we show the force constants k_x (along the polarization axis), k_y, and k_z (along the propagation axis) normalized to the power at the sample (15 mW). Particles in sample 4 with an average size of ∼750 nm are trapped with force constants as high as 10 pN/nmW, the largest trapped particle size for this sample. Error bars on the abscissas are the results of TEM analysis (see text). Data are well fitted with a power law scaling, from which we can get a slope $\alpha \approx 1.6$ taken as the average of the fitted exponents for the three data sets. The purple solid line is the theory for spherical particles[30] optically trapped at 830 nm. The yellow regions are defined by the maximum trapping efficiency and radius obtained in experiments with gold spherical particles.[24,29] The yellow stars are the calculated values for the model cluster A shown in Figure 6a.

cross sections (solid lines for cluster A, B, C) compared to the experimental extinction spectrum (dashed line). Note that the measured extinction is an ensemble average resulting from the different optical properties of the AuNPAs in the sample, thus we would need to average over all possible cluster configurations to have a match with the measured UV−vis spectrum. The radiation force constants are derived as the first derivatives of the force with respect to position calculated at the equilibrium position and orientation (see Methods). For the cluster with the long wavelength plasmon resonance closest to the experiment, cluster A in Figure 6 panel a, we obtain $k_x = 0.1$, $k_y = 0.16$, and $k_z = 0.03$ pN/nmW. These calculated values (yellow stars in Figure 5) are in fair agreement with the averaged experimental ones relative to sample 2 (red data in Figure 5). Furthermore they are 10 times larger than the force constants on the subunits composing the cluster and 3 times larger than those exerted on a sphere with the cluster equivalent volume. Thus the striking increase in the measured force constants with the growth of the AuNPAs can be understood with three major effects occurring when aggregation takes place. First of all, the trapped particle volume increases leading to a larger force with respect to the individual spherical subunits.[18,30,53] More important, the aggregation yields a long wavelength plasmon resonance that shifts closer to the trap-
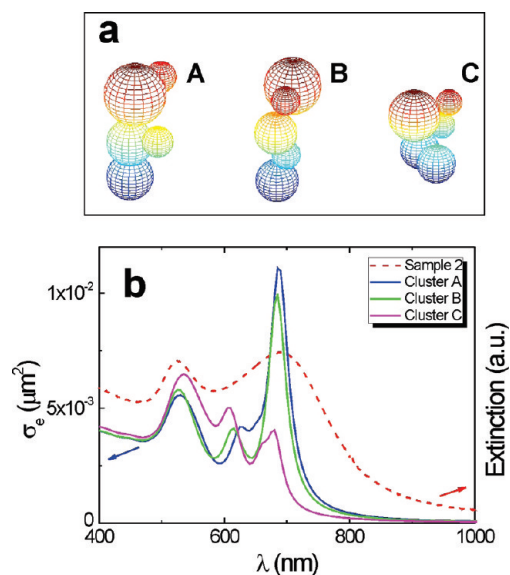
Figure 6. (a) Models of gold nanoaggregates as clusters of spherical nanoparticles built starting from the TEM images from our samples (for example, see Figure 1d). We calculate the extinction cross-section (b) and compare it with the experimental extinction, sample 2 in this case. Note that the measured extinction is an average resulting from the different optical properties of the aggregates in the ensemble. After a matching between the model with the TEM and the long wavelength plasmonic resonance, we calculate the radiation force finding good agreement with the optical trapping measurements.

ping wavelength (Figure 1b and Figure 5a). Thus, for AuNPAs, this plasmon resonance drives the trapping mechanism, enhancing further the efficiency. Finally, the fractal structure of AuNPAs results in a reduced absorption with respect to a spherical particle of comparable size. Hence radiation pressure, that limits the trapping range for individual spherical particles,[24,29,30] is reduced for trapped AuNPAs contributing to the enhancement of the trapping efficiency. The role of fractal structure is also evidenced by checking the size scaling of the force constants, that is, fitting the data in Figure 5b−d with a power law r^{α}. For individual spherical particles with radii below 50 nm, volume scaling, that is, $\alpha = 3$, has been experimentally and theoretically demonstrated.[24,29,30] For larger spherical particles (up to the limit of $r \approx 125$ nm), a regime where $\alpha \approx 2$, that is, a surface scaling, has also been experimentally investigated,[24,29] although a clear theoretical understanding of this scaling law is still missing.[30] For the case of AuNPAs the force constants are fitted (dashed blue lines in Figure 5b−d) by a scaling with $\alpha \approx 1.6$ indicating a role of the multiple scattering of light within the fractal aggregates.

CONCLUSIONS

We have shown that gold nanoaggregates of controlled size and properties can be stably trapped with optical tweezers working in the near-infrared. Plasmonic nanostructures made by AuNPs with selected extinction properties and average radii in the 20−750 nm range were obtained by a two-step procedure consisting in LASiS of AuNPs and their controlled aggregation. The strong field-enhancement driven by the nanoaggregates yields an increase in the trapping efficiency by a factor of 50 higher than previously reported for individual spherical gold nanoparticles. Force constants of the order of 10 pN/nmW were measured for the largest aggregates with 750 nm average radius. These larger trapping efficiencies and the wider particle size range open perspectives for the use of gold nanoaggregates as improved local Raman probes in liquid environment with a three-dimensional position control at the nanometer scale, as well as nanohandles for *in vivo* manipulation of larger biological material.

METHODS

LASiS. Gold nanoparticles (AuNPs) in water were obtained by laser ablation synthesis in solution (LASiS) with 1064 nm (9 ns) laser pulses of a Q-switched Nd:YAG laser (Quantel YG981E) focused with a lens ($f = 10$ cm) on a gold (99.99%) plate placed at the beam focus on the bottom of a cell containing bidistilled water.[39] We used pulses in the range of 10 J cm^2 at 10 Hz repetition rate for 30 min. The concentration of AuNPs was evaluated by fitting the UV−vis spectra with a Mie−Gans model.[40]

Controlled Aggregation. Concentrations of 0.01 μL/mL (sample 2), 0.05 μL/mL (sample 3) and 0.25 μL/mL (sample 4) of pyridine (Sigma Aldrich) were added to 2 nM AuNPs solutions as obtained by LASiS. All solutions were kept under vigorous stirring during the addition. After 30 min, 0.1 mg/mL of BSA (Sigma Aldrich) were added to the solutions of aggregated AuNPs and to nonaggregated AuNPs. Excess pyridine and BSA were removed by centrifugation.

Samples Characterization. The solutions were characterized by UV−vis spectroscopy with a Varian Cary 5 spectrometer and transmission electron microscopy (TEM) at 300 kV with a JEOL JEM 3010 microscope equipped with a Gatan Multiscan CCD camera model 794. TEM samples were prepared by depositing one drop of the solution on a copper grid covered with a holey carbon film.

Optical Tweezers. Optical trapping is accomplished by tightly focusing a laser beam through an oil immersion high numerical aperture objective (Olympus, Uplan FLN 100X, NA = 1.3). We use a 830 nm, 150 mW laser diode (Sanyo DL-8032-01) as a radiation source. The laser beam is circularized by a pair of anamorphic prisms. A 1:4 telescope is used to enlarge the beam so as to overfill the microscope objective back aperture and to yield a diffraction limited spot of about 0.64 μm in its focal plane. The optical setup is built in an inverted configuration that gives more stability because it helps to counteract gravity with radiation pressure for weak traps. Beam steering can be achieved through a pair of orthogonally mounted, computer controlled galvomirrors so that dynamic multiple traps and time-averaged traps can be created *via* time-sharing of the trapping beam.[57] Samples are placed in a small chamber with 75 μL volume attached on the microscope stage. A CCD camera is used to image the trapped particles. Image calibration is achieved by

optical trapping size-standard latex beads (Polysciences) and by imaging a calibrated microscope microgrid.

Particle tracking. Particle tracking and force sensing are obtained through back focal plane interferometry,[47] where the interference pattern from the scattered and unscattered light by the trapped particle is collected onto a quadrant photodiode (QPD) that in our setup is also oriented with the polarization (x-)axis.[17,19] When the particle is centered with the trap, each quadrant generates equal photocurrents, while when the particle moves from the center, the outputs Q_i from all quadrants are changed. Combining these signals as pairwise sums it is possible to generate signals S_x, S_y, S_z proportional to the trapped particle's displacements in the three directions (x, y, z) defined by the trapping potential (*e.g.*, $S_x = [Q_1 + Q_4] - [Q_2 + Q_3] \propto x$). For each experiment the positional data were recorded with an acquisition board (National Instruments) at a sampling rate of 50 kHz for 2 s (10^5 points per channel) using a custom-made LabView program.

Theory. The starting point of our procedure is the formulation by Richards and Wolf[58] of the field configuration in the focal region of a high numerical aperture (fixed to be NA = 1.3 as in our experiments) objective lens in absence of any particle. The resulting field is the field incident on the particles, and the radiation force exerted on any particle within the region is calculated by resorting to linear and angular momentum conservation for the combined system of field and particles. We adopt a geometry such that the coordinate systems *Oxyz* is linked to the laboratory, and *O′x′y′z′* is linked to the local frame of reference with origin in the center of mass of the aggregate.[52,53] Thus the optical force and torque exerted on a particle turn out to be[18,30,53]

$$\mathbf{F}_{Rad} = r^2 \int_{\Omega} \mathbf{\hat{r}} \cdot \langle \mathbf{T_M} \rangle \, d\Omega \qquad (2)$$

$$\mathbf{M}_{Rad} = -r^3 \int_{\Omega} \mathbf{\hat{r}} \cdot \langle \mathbf{T_M} \rangle \times \mathbf{\hat{r}} \, d\Omega \qquad (3)$$

where the integration is over the full solid angle, r is the radius of a large sphere surrounding the particle center of mass, and $\langle \mathbf{T_M} \rangle$ is the time averaged Maxwell stress in the form of Minkowski.[59] No inconvenience comes from this choice because the external

medium is isotropic, thus

$$\langle \mathbf{T_M} \rangle = \frac{1}{8\pi} Re\left[n^2 \mathbf{E} \otimes \mathbf{E}^* + \mathbf{B} \otimes \mathbf{B}^* - \frac{1}{2}(n^2|\mathbf{E}|^2 + |\mathbf{B}|^2)\mathbf{I} \right] \quad (4)$$

where $\otimes$ denotes dyadic product, I is the unit dyadic, and n is the refractive index of the surrounding medium. When the incident field is a polarized plane wave, the components of the radiation force along the direction of the unit vector $\mathbf{v}_\xi$ are given by[53]

$$\mathbf{F}_{rad\xi} = -\frac{r^2}{16\pi} Re \int (\hat{\mathbf{r}} \cdot \hat{\mathbf{v}}_\xi)[n^2(|\mathbf{E}_S|^2 + 2\mathbf{E}_I \cdot \mathbf{E}_S) + (|\mathbf{B}_S|^2$$
$$+ 2\mathbf{B}_I \cdot \mathbf{B}_S)] \, d\Omega \quad (5)$$

where $\mathbf{E}_I$ and $\mathbf{B}_I$ are the incident fields, while $\mathbf{E}_s$ and $\mathbf{B}_s$ are the fields scattered by the particle. In turn the radiation torque takes on the form:

$$\mathbf{M}_{rad} = \frac{1}{8\pi} r^3 Re \int n^2 \hat{\mathbf{r}} \cdot (\mathbf{E}_I + \mathbf{E}_S)(\mathbf{E}_I + \mathbf{E}_S) \times \hat{\mathbf{r}} \, d\Omega \quad (6)$$

Expanding the incident field in a series of vector spherical harmonics with (known) amplitudes $W^p_{1\,lm}$, the scattered field can be expanded on the same basis with amplitudes $A^{p'}_{l'm'}$. The relation between the two amplitudes is given by $A^{p'}_{l'm'} = \sum_{plm} S^{p'p}_{l'm'lm} W^p_{1\,lm}$, where $S^{p'p}_{l'm'lm}$ is the T-matrix of the particle. The elements of the T-matrix are calculated in a given frame of reference through the inversion of the matrix of the linear system obtained by imposing to the fields boundary conditions across each spherical surface.[44] Each element of the T-matrix turns out to be independent both of the direction of propagation and of the polarization of the incident field. Thus they do not change when the incident field is a superposition of plane waves with different direction of propagation, that is, for the description of a focused laser beam in the angular spectrum representation.[60]

We modeled AuNPAs as clusters of spherical subunits, whose dimensions are chosen so that the wavelength of their longitudinal plasmon resonance corresponds to the experimental one. The TEM images suggest that the subunits have different radii, ranging from 5 up to 30 nm, thus we adopted this range of dimensions in our models. We calculate for each cluster the radiation force $\mathbf{F}_{rad}(\mathbf{R})$ and torque $\mathbf{M}_{rad}(\mathbf{R})$, the argument $\mathbf{R}$ denoting the position of the center of mass of the aggregate. The trapping occurs on the optical axis[18,53] where all the components of force and torque vanish with a negative derivative. In the vicinity of the trapping point $R_0 = (0,0,z_0)$ the components of $\mathbf{F}_{rad}(\mathbf{R})$ can be approximated by $F_{rad_x}(x,0,z_0) = -k_x x$, $F_{rad_y}(0,y,z_0) = -k_y y$, $F_{rad_z}(0,0,z) = -k_z(z - z_0)$. Where k_x, k_y, and k_z are the force constants. Thus we first determine the trapping position and equilibrium orientation of the cluster, and then calculate the force constants around this equilibrium state.

The number of subunits composing the cluster are limited by the memory demand of the computing facilities. In fact the calculation of the transition matrix for a N-sphere aggregate, requires the inversion of a matrix of order $d = 2N \times l_T(l_T + 2)$, where l_T is the l-value at which the multipole expansion of the electromagnetic fields is truncated.[52] To ensure the numerical stability of the results, that depends on the size of both the subunits and of the aggregate as a whole, we check each aggregate for the existence of an l-value l_M for which, if $l_T > l_M$, the extinction cross-section does not change. For the gold aggregates of Figure 6 with 5 subunits, this generally happened for an l_M of the order of 14. This value is related to the internal fields of the subunits that include also the longitudinal field described by Ruppin[61] and dealt through the longitudinal dielectric function of Lindhard,[55] as corrected by Pack.[56] The transition matrix then contains (2240×2240) complex elements. Calculations of extinction cross sections, radiation force, and torque were performed on a HP/Itanum 2 cluster, requiring about 2 h of CPU time for every configuration with a memory demand of about 0.4 GByte. In contrast, for an aggregate with for example, 100 subunits that would represent an AuNPA in sample 3 or sample 4, we would expect an l_M of the order of 140 to be required, yielding $((4 \times 10^6) \times (4 \times 10^6))$ complex elements, which would need about 1 PB of memory, far beyond any computer facility capabilities.

Supporting Information Available: Movie 1: A gold nanoaggregate with an asymmetric morphology is optically trapped. Continuous rotation is observed as a consequence of the particle shape, that is, anisotropic scattering causes rotation about the laser propagation direction (the so-called "windmill effect"). Movie 2: When using the maximum power (32 mW on the sample) we observed strong heating and bubbling when trapping large (micro) aggregates. In the movie a bubble grows soon after an aggregate from sample 3 is drawn into the trap, the growth lasts few seconds, until the bubble reaches a size of about 5—6 μm and the growth stops. This material is available free of charge *via* the Internet at http://pubs.acs.org.

REFERENCES AND NOTES

1. Maier, S. A. *Plasmonics: Fundamentals and Applications*; Springer: New York, 2007.
2. Brongersma, M. L.; Kik, P. G. *Surface Plasmon Nanophotonics*; Springer Series in Optical Sciences; Springer: Dordrecht, The Netherlands, 2007.
3. Mafuné, F.; Kohno, J.; Takeda, T.; Kondow, T. Full Physical Preparation of Size-Selected Gold Nanoparticles in Solution: Laser Ablation and Laser-Induced Size Control. *J. Phys. Chem. B* **2002,** *106*, 7575–7577.
4. Wang, Y.; Xie, X.; Goodson, T., III. Enhanced Third-Order Nonlinear Optical Properties in Dendrimer–Metal Nano-composites. *Nano Lett.* **2005,** *5*, 2379–2384.
5. Yang, G. W. Laser Ablation in Liquids: Applications in the Synthesis of Nanocrystals. *Progr. Mater. Sci.* **2007,** *52*, 648–698.
6. Compagnini, G.; Messina, E.; Puglisi, O.; Cataliotti, R. S.; Nicolosi, V. Spectroscopic Evidence of a Core–Shell Structure in the Earlier Formation Stages of Au–Ag Nanoparticles by Pulsed Laser Ablation in Water. *Chem. Phys. Lett.* **2008,** *457*, 386–390.
7. Menéndez-Manjòn, A.; Chichkov, B. N.; Barcikowski, S. Influence of Water Temperature on the Hydrodynamic Diameter of Gold Nanoparticles from Laser Ablation. *J. Phys. Chem. C* **2010,** *114*, 2499–2504.
8. Liu, P.; Cui, H.; Wang, C. X.; Yang, G. W. From Nanocrystal Synthesis to Functional Nanostructure Fabrication: Laser Ablation in Liquid. *Phys. Chem. Chem. Phys.* **2010,** *12*, 3942–3952.
9. Kreibig, U.; Vollmer, M. *Optical Properties of Metal Clusters*; Springer Series in Material Science, Vol 25; Springer:Berlin; New York, 1995.
10. Kneipp, K., Moskovits, M., Kneipp, H., Eds. Surface-Enhanced Raman Scattering: Physics and Applications, Springer: New York, 2006.
11. Xu, H.; Bjerneld, E. J; Kall, M.; Börjesson, L. Spectroscopy of Single Hemoglobin Molecules by Surface-Enhanced Raman Scattering. *Phys. Rev. Lett.* **1999,** *83*, 4357–4360.
12. Ashkin, A.; Dziedzic, J. M.; Bjorkholm, J. E.; Chu, S. Observation of a Single-Beam Gradient Force Optical Trap for Dielectric Particles. *Opt. Lett.* **1986,** *11*, 288.
13. Ashkin, A. *Optical Trapping and Manipulation of Neutral Particles Using Lasers*; World Scientific Publishing: Singapore, 2006.
14. Grier, D. G. A Revolution in Optical Manipulation. *Nature* **2003,** *424*, 810–816.
15. Maragò, O. M.; Jones, P. H.; Gucciardi, P. G. Photonic Force Microscopy: From Femtonewton Force Sensing to Ultra-sensitive Spectroscopy. *Scanning Probe Microscopy in Nanoscience and Nanotecnology*; Bushan, B., Ed.; Springer-Verlag: Berlin, 2010.
16. Nakayama, Y.; Pauzauskie, P. J.; Radenovic, A.; Onorato, R. M.; Saykally, R. J.; Liphardt, J.; Yang, P. Tunable Nanowires Nonlinear Optical Probe. *Nature* **2007,** *447*, 1098–1102.
17. Maragò, O. M.; Jones, P. H.; Bonaccorso, F.; Scardaci, V.; Gucciardi, P. G.; Rozhin, A.; Ferrari, A. C. Femtonewton Force Sensing with Optical Trapped Nanotubes. *Nano Lett.* **2008,** *8*, 3211–3216.

18. Borghese, F.; Denti, P.; Saija, R.; Iatí, M. A.; Maragò, O. M. Radiation Force and Torque on Optically Trapped Linear Nanostructures. *Phys. Rev. Lett.* **2008,** *100,* 163903.

19. Jones, P. H.; Palmisano, F.; Bonaccorso, F.; Gucciardi, P. G.; Calogero, G.; Ferrari, A. C.; Maragó, O. M. Rotation Detection in Light-Driven Nanorotors. *ACS Nano* **2009,** *3,* 3077–3084.

20. Neves, A. A. R.; Camposeo, A.; Pagliara, S.; Saija, R.; Borghese, F.; Denti, P.; Iatì, M. A.; Cingolani, R.; Maragò, O. M.; Pisignano, D. Rotational Dynamics of Optically Trapped Nanofibers. *Opt. Express* **2010,** *18,* 822–830.

21. Petrov, D. V. Raman Spectroscopy and Optically Trapped Particles. *J. Opt. A: Pure Appl. Opt.* **2007,** *9,* S139–S156.

22. Maragò, O. M.; Bonaccorso, F.; Saija, R.; Privitera, G.; Gucciardi, P. G.; Iatì, M. A.; Calogero, G.; Jones, P. H.; Borghese, F.; Denti, P.; *et al.* Brownian Motion of Graphene. *ACS Nano* **2010,** *4,* 7515–7523.

23. Svoboda, K.; Block, S. M. Optical Trapping of Metallic Rayleigh Particles. *Opt. Lett.* **1998,** *28,* 930–932.

24. Hansen, P. M.; Bhatia, V. K.; Harrit, N.; Oddershede, L. Expanding the Optical Trapping Range of Gold Nanoparticles. *Nano Lett.* **2005,** *5,* 1937–1942.

25. Seol, Y; Carpenter, A. E.; Perkins, T. T. Gold Nanoparticles: Enhanced Optical Trapping and Sensitivity Coupled with Significant Heating. *Opt. Lett.* **2006,** *31,* 2429–2431.

26. Pelton, M.; Liu, M.; Kim, H. Y.; Smith, G.; Guyot-Sionnest, P.; Scherer, N. F. Optical Trapping and Alignment of Single Gold Nanorods by Using Plasmon Resonances. *Opt. Lett.* **2006,** *31,* 2075.

27. Bosanac, L.; Aabo, T.; Bendix, P. M.; Oddershede, L. B. Efficient Optical Trapping and Visualization of Silver Nanoparticles. *Nano Lett.* **2008,** *8,* 1486–1491.

28. Selhuber-Unkel, C.; Zins, I.; Schubert, O.; Sönnichsen, C.; Oddershedde, L. B. Quantitative Optical Trapping of Single Gold Nanorods. *Nano Lett.* **2008,** *8,* 2998–3003.

29. Hajizadeh, F.; Reihani, S. N. S. Optimized Optical Trapping of Gold Nanoparticles. *Opt. Exp.* **2010,** *18,* 551–559.

30. Saija, R.; Denti, P.; Borghese, F.; Maragò, O.; Iatì, M. A. Optical Trapping Calculations for Metal Nanoparticles. Comparison with Experimental Data for Au and Ag Spheres. *Opt. Exp.* **2009,** *17,* 10231–10241.

31. Arias-González, J. R.; Nieto-Vesperinas, M. Optical Forces on Small Particles: Attractive and Repulsive Nature and Plasmon-Resonance Conditions. *J. Opt. Soc. Am. A* **2003,** *20,* 1201–1209.

32. Toussaint, K. C.; Liu, M.; Pelton, M.; Pesic, J.; Guffey, M. J.; Guyot-Sionnest, P.; Scherer, N. F. Plasmon Resonance-Based Optical Trapping of Single and Multiple Au Nanoparticles. *Opt. Exp.* **2007,** *15,* 12017–12029.

33. Guffey, M. J.; Scherer, N. F. All-Optical Patterning of Au Nanoparticles on Surfaces Using Optical Traps. *Nano Lett.* **2010,** *10,* 4302–4308.

34. Gaugiran, S.; Getin, S.; Fedeli, J. M.; Derouard, J. Polarization and Particle Size Dependence of Radiative Forces on Small Metallic Particles in Evanescent Optical Fields. Evidences for either Repulsive or Attractive Gradient Forces. *Opt. Exp.* **2007,** *15,* 8146–8156.

35. Dienerowitz, M.; Mazilu, M.; Reece, P. J.; Krauss, T. F.; Dholakia, K. Optical Vortex Trap for Resonant Confinement of Metal Nanoparticles. *Opt. Exp.* **2008,** *16,* 4991–4999.

36. Bendix, P. M.; Reihani, S. N.; Oddershede, L. B. Direct Measurements of Heating by Electromagnetically Trapped Gold Nanoparticles on Supported Lipid Bilayers. *ACS Nano* **2010,** *4,* 2256–2262.

37. Liu, Z.; Hung, W. H.; Aykol, M.; Valley, D.; Cronin, S. B. Optical Manipulation of Plasmonic Nanoparticles, Bubbles Formation and Pattering of SERS Aggregates. *Nanotechnology* **2010,** *21,* 105304–105308.

38. Zhang, Y.; Gu, C.; Schwartzberg, A. M.; Chen, S.; Zhang, J. Z. Optical Trapping and Light-Induced Agglomeration of Gold Nanoparticle Aggregates. *Phys. Rev. B* **2006,** *73,* 165405.

39. Amendola, V.; Meneghetti, M. Controlled Size Manipulation of Free Gold Nanoparticles by Laser Irradiation and Their Facile Bioconjugation. *J. Mater. Chem.* **2007,** *17,* 4705–4710.

40. Amendola, V.; Meneghetti, M. Size Evaluation of Gold-Nanoparticles by UV−Vis Spectroscopy. *J. Phys. Chem. C.* **2009,** *113,* 4277–4285.

41. Amendola, V.; Meneghetti, M. Laser Ablation Synthesis in Solution and Size Manipulation of Noble Metal Nanoparticles. *Phys. Chem. Chem. Phys.* **2009,** *11,* 3805–3821.

42. Blatchford, C. G.; Campbell, J. R.; Creighton, J. A. Plasma Resonance-Enhanced Raman Scattering by Absorbates on Gold Colloids: The Effect of Aggregation. *Surf. Sci.* **1982,** *120,* 435–455.

43. Galletto, P.; Brevet, P. F.; Girault, H. H.; Antoine, R.; Broyer, M. Enhancement of the Second Harmonic Response by Absorbates on Gold Colloids: The Effect of Aggregation. *J. Phys. Chem. B* **1999,** *103,* 8706–8710.

44. Park, S. Y.; Lee, J.-S.; Georganopoulou, D.; Mirkin, C. A.; Schatz, G. C. Structures of DNA-Linked Nanoparticle Aggregates. *J. Phys. Chem. B* **2006,** *110,* 12673–12681.

45. Singer, W.; Nieminen, T. A.; Gibson, U. J.; Heckenberg, N. R.; Rubinsztein-Dunlop, H. Orientation of Optically Trapped Nonspherical Birefringent Particles. *Phys. Rev. E* **2006,** *73,* 021911.

46. Galajda, P.; Ormos, P. Complex Micromachines Produced and Driven by Light. *Appl. Phys. Lett.* **2001,** *78,* 249–251.

47. Pralle, A.; Prummer, M.; Florin, E.-L.; Stelzeer, E. H. K.; Horber, J. K. H. Three-Dimensional High-Resolution Particles Tracking for Optical Tweezers by Forward Scattered Light. *Microsc. Res. Technol.* **1999,** *44,* 378–386.

48. Rohrbach, A. Stiffness of Optical Traps: Quantitative Agreement between Experiment and Electromagnetic Theory. *Phys. Rev. Lett.* **2005,** *95,* 168102.

49. Volpe, G.; Petrov, D. Torque Detection Using Brownian Fluctuations. *Phys. Rev. Lett.* **2006,** *97,* 210603.

50. Martin, S.; Reichert, M.; Stark, H.; Gisler, T. Direct Observation of Hydrodynamic Rotation−Translation Coupling between Two Colloidal Spheres. *Phys. Rev. Lett.* **2006,** *97,* 248301.

51. Broersma, S. Viscous Force and Torque Constants for a Cylinder. *J. Chem. Phys.* **1981,** *74,* 6989.

52. Borghese, F.; Denti, P.; Saija, R. *Scattering from Model Nonspherical Particles*, 2nd ed.; Springer: Berlin, 2007.

53. Borghese, F.; Denti, P.; Saija, R.; Iatì, M. A. Optical Trapping of Nonspherical Particles in the T-Matrix Formalism. *Opt. Express* **2007,** *15,* 11984.

54. Johnson, P. B.; Christy, R. W. Optical Constants of the Noble Metals. *Phys. Rev. B* **1972,** *6,* 4370.

55. Lindhard, J. On The Properties Of A Gas Of Charged Particles. *R. Danish Acad. Sci. Lett.: Math.-Fys. Medd.* **1954,** *28,* 8.

56. Pack, A.; Hietschold, M.; Wannemacher, R. Failure of Local Mie Theory: Optical Spectra of Colloidal Aggregates. *Opt. Commun.* **2001,** *194,* 277–287.

57. Maragò, O. M.; Gucciardi, P. G.; Bonaccorso, F.; Calogero, G.; Scardaci, V.; Rozhin, A. G.; Ferrari, A. C.; Jones, P. H.; Saija, R.; Borghese, F.; *et al.* Optical Trapping of Carbon Nanotubes. *Phys. E* **2008,** *8,* 2347–2351.

58. Richards, B.; Wolf, E. Electromagnetic Diffraction in Optical Systems II. Structure of the Image Field in an Aplanatic System. *Proc. R. Soc. London, Ser. A* **1959,** *253,* 358.

59. Pfeifer, R. N.; Nieminen, T. A.; Heckenberg, N. R.; Rubinsztein-Dunlop, H. Momentum of an Electromagnetic Wave in Dielectric Media. *Rev. Mod. Phys.* **2007,** *79,* 1197–1216.

60. Novotny, L.; Hecht, B. *Principles of Nano-Optics*; Cambridge University Press: New York, 2006.

61. Ruppin, R. Optical Properties of Small Metal Spheres. *Phys. Rev. B* **1975,** *11,* 2871.